Manipulating Fermi arc surface states for nonlinear nonreciprocal transport in Weyl semimetals

K. X. Jia,[1] R. Ma,[2] H. Geng[1,3,*] L. Sheng,[1,3,†] and D. Y. Xing[1,3]

[1]*National Laboratory of Solid State Microstructures and Department of Physics, Nanjing University, Nanjing 210093, China*
[2]*Nanjing University of Information Science and Technology, Nanjing 210044, China*
[3]*Collaborative Innovation Center of Advanced Microstructures, Nanjing University, Nanjing 210093, China*

In this work, the realization of nonreciprocal transport in Weyl semimetals is proposed by manipulating surface states. Our method, distinct from traditional techniques focusing on bulk band asymmetry, involves surface asymmetries characterized by an asymmetric mass term. Utilizing the Boltzmann transport equation, we unveil second-order conductivity responses, leading to nonreciprocal transport primarily governed by Fermi arc surface states when the Fermi surface is proximal to the Weyl point. Our method deviates from conventional techniques focused on bulk band asymmetry, shedding light on distinctive transport properties from engineering surface states in Weyl semimetals. Importantly, our findings provide an observable signal for surface state engineering, enhancing the understanding of nonlinear transport phenomena in these topological semimetals.

I. INTRODUCTION

Reciprocity in charge transport reflects a symmetrical interplay between current and voltage, where the current magnitude induced by a positive voltage equals that generated by a corresponding negative voltage. This reciprocity is typically protected by time-reversal symmetry (TRS) and spatial inversion symmetry (SIS) [1], thereby rendering it a prevalent phenomenon in natural systems. Conversely, systems that exhibit nonreciprocal behaviors have garnered significant interest, such as the pn junction. Contrasting with the inherently asymmetric nature of pn junctions, achieving nonreciprocal transport in materials with translational symmetry remains a challenge. The pioneering concept of electric magnetochiral anisotropy and unidirectional magnetoresistance introduced by Rikken [2] has sparked extensive research into materials exhibiting nonreciprocal transport, leading to discoveries in systems like chiral nanosystems [2,3], polar semiconductors [4–6], bilayer heterojunctions [7–11], and topological systems [12,13]. Nonreciprocal responses can arise from either linear or nonlinear processes, with the latter being more complex and currently under active development [1].

Topological semimetals, recognized as a novel class of topological materials [14–31], have sparked notable interest in the study of nonlinear transport phenomena [14,32–43]. The pursuit of nonlinear transports in topological semimetals is also fundamentally associated with breaking TRS or SIS. In Weyl semimetals, the inherent absence of at least one of these symmetries makes them particularly suitable for studies in nonlinear transport. Theoretically, the Boltzmann equation, combined with the band-geometric quantities, provides an effective method for exploring nonlinear electrical and thermal transport in such systems [32,44–46]. Based on the semiclassical Boltzmann transport formalism, a specific tilt in the band structure is essential for simultaneously breaking intravalley and intervalley symmetries [32,43], which constrains the scope of potential candidates. On the other hand, the Fermi arc surface states (FAs) are a hallmark of Weyl semimetals. Interestingly, recent research progress shows that the configurations of the FAs are quite sensitive to the details of the sample boundary, which opens the possibility for manipulating the FAs through surface modifications [47–51]. Moreover, advances in surface engineering and chemical doping have enabled modifications to the chemical potential of surface states, while preserving the lattice structure and symmetry [52]. These advancements render the nonreciprocal transport induced by the asymmetry of FAs a promising area of research. An interesting question is whether the chirality of the FAs manifests itself through surface state engineering and causes the related nonlinear effect [12,41]

In this work, we propose an interesting approach for nonlinear nonreciprocal transports in Weyl semimetals. Distinct from modulating the bulk band structures, we use the FAs of Weyl semimetals to realize nonreciprocal transport, obviating the symmetry requirements of the bulk band. As shown in Fig. 1(a), the FAs on the upper and lower surfaces converge at the projection of the Weyl points, displaying opposite group velocities. This topologically protected spatial separation of electrons moving in opposite directions facilitates the creation of asymmetric energy bands through the manipulation of FAs. The key point to our model is the use of an effective potential by surface doping on a specific surface state, while preserving the bulk band structure, as shown in Fig. 1(c). This approach results in the emergence of a significant second-order conductivity which shows a proportional relationship with the square of the relaxation time, the applied effective potential, and the chemical potential. Additionally, the nonreciprocal transport signals are theoretically calculated in a Weyl semimetal

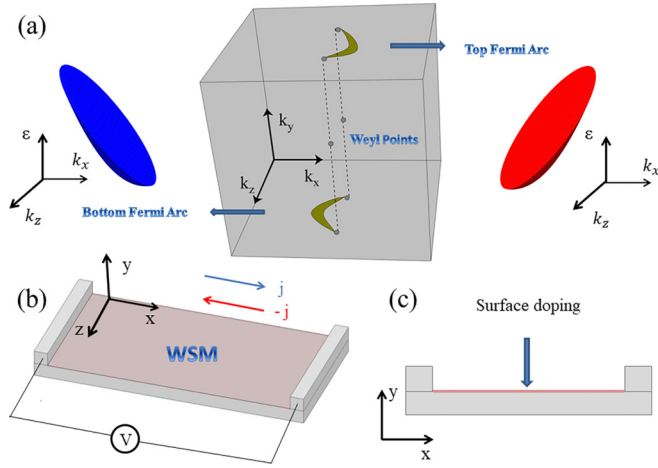_____
*genghao@nju.edu.cn
†shengli@nju.edu.cn

FIG. 1. (a) shows the schematic representation of a Weyl semimetal, illustrating a pair of Weyl points and their surface projections connected by FAs. The surface states exhibit chiral dispersion, with electrons on opposing surfaces moving at opposite velocities and interconnected through the bulk Weyl points. (b) and (c) show the proposed model for measuring nonreciprocal transport in a Weyl semimetal nanobelt. The red area indicates the doping on the upper surface which modulates the effective potential.

nanobelt, as shown in Fig. 1(b). Attributed to the suppression of backward scattering in the FAs, the current discrepancy for opposing voltages achieves an order of magnitude of 10^{-1}, which provides a distinct signal for surface state engineering.

The remainder of the paper is organized as follows. In Sec. II, the model Hamiltonian and the Boltzmann equation method was introduced. In Sec. III, the numerical results were presented and the behavior of the nonlinear conductivity was discussed. The summary and discussion are given in Sec. IV.

II. MODEL AND METHOD

A. Boltzmann equation and symmetry analysis

We begin with the steady-state Boltzmann equation under the relaxation time approximation

$$eE \cdot \nabla_k f = -\frac{f - f_0}{\tau}, \tag{1}$$

where f_0 is the Fermi-Dirac distribution function of the electrons, E is the electric field, and τ is the average scattering time between two successive collisions, which is assumed to be a constant. The electron current is expanded to the second order of the electric field as

$$j = \sigma_1 E + \sigma_2 E^2 \tag{2}$$

where j denotes the current density. The second-order term of the electric field does not vary with the direction, and thus gives rise to a nonreciprocal current after reversing the direction of the field. To calculate the nonlinear transport coefficients, the distribution function is also expanded to the second-order of the electric field

$$f = f_0 + f_1 + f_2. \tag{3}$$

Substituting it into Eq. (1) and comparing the same order terms of E, the following equations can be obtained:

$$\begin{aligned} f_1 &= -\tau e E \cdot \nabla_k f_0 \\ f_2 &= -\tau e E \cdot \nabla_k f_1. \end{aligned} \tag{4}$$

In our study, we implement an electric field along the x axis and concentrate our investigation on longitudinal transport. After some straightforward algebra, we can obtain

$$f_2 = \tau^2 e^2 E_x^2 \left(\frac{\partial v_x}{\partial k_x} \frac{\partial f_0}{\partial \varepsilon} + v_x^2 \frac{\partial^2 f_0}{\partial^2 \varepsilon} \right). \tag{5}$$

Defining

$$\begin{aligned} j_x &= \sigma_1 E_x + \sigma_2 E_x^2 \\ &= e \int v_x f_1 dk_x + e \int v_x f_2 dk_x, \end{aligned} \tag{6}$$

we obtain the electron conductivities σ_1 and σ_2:

$$\sigma_1 = e^2 \tau \int v_x^2 \left(-\frac{\partial f_0}{\partial \varepsilon} \right) dk_x$$

$$\begin{aligned} \sigma_2 &= \frac{e^3 \tau^2}{\hbar} \int v_x \left(\frac{\partial v_x}{\partial k_x} \frac{\partial f_0}{\partial \varepsilon} + v_x^2 \frac{\partial^2 f_0}{\partial^2 \varepsilon} \right) dk_x \\ &= \frac{e^3 \tau^2}{\hbar} \int v_x \frac{\partial v_x}{\partial k_x} \left(-\frac{\partial f_0}{\partial \varepsilon} \right) dk_x, \end{aligned} \tag{7}$$

where $v_x = \frac{\partial \varepsilon}{\partial k_x}$ and integration by parts has been applied. These equations suggest that a nonzero σ_2 necessitates an energy spectrum that is not an even function of k_x. This reflects the requirements for the system's symmetry, especially in terms of SIS and TRS. Under time reversal or spatial inversion operations, both k_x and v_x change sign. Therefore, the linear conductivity σ_1 can be nonzero but the second order conductivity σ_2 is forced to vanish. In Weyl semimetals, electrons moving in opposite directions are spatially separated, and distributed on the opposing FAs, as shown in Fig. 1. This unique topological property enables us to achieve asymmetry in the complete bands of the two surface states by surface engineering, without altering the bulk energy bands [52].

B. Model Hamiltonian

Merely fulfilling the previously mentioned symmetry requirements is not sufficient to realize nonlinear conductivity. A nonlinear dispersion of the bulk band is also essential. Otherwise, the dispersion of the Fermi arc surface states would be linear, resulting in the term $\frac{\partial v_x}{\partial k_x} = 0$ in Eq. (7). From the semiclassical Boltzmann approach, the drift in the first order electron distribution function f_1 induced by an electric field is proportional to $\frac{\partial f_0}{\partial k_x}$, which becomes zero when $v_x = \frac{\partial \varepsilon}{\partial k_x} = 0$. Similarly, the second-order distribution f_2 could be regarded as the drift of the first-order distribution f_1 driven by the electric field, requiring a nonzero $\frac{\partial^2 \varepsilon}{\partial k_x^2}$.

Based on our analysis, the following model of Weyl semimetals were considered, which is widely recognized in the study of magnetotransport and the three-dimensional quantum Hall effect [53]

$$H(k) = C_1(k_x^2 + k_z^2) + C_2(k_x \sigma_x + k_y \sigma_y) + C_3(k_w^2 - k^2)\sigma_z. \tag{8}$$
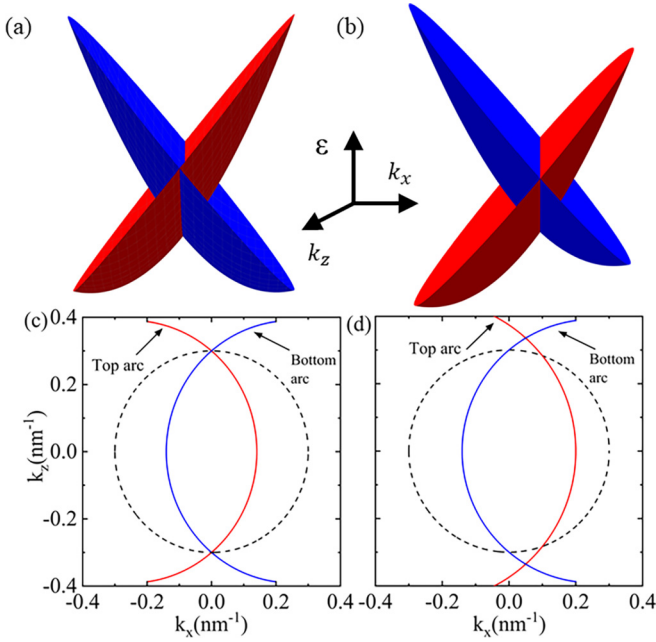
FIG. 2. Dispersion of the FAs. (a) and (b) display the band structure before and after doping, respectively. The top and bottom bands are depicted using red and blue colors, exhibiting symmetrical and asymmetrical behaviors against k_x. (c) and (d) depict the FAs at $E_w = C_1 k_w^2$, where in (c) the arcs are symmetric around k_x, while in (b) the top arc shows divergence. The regions of the FAs are indicated by black dashed circles.

$(\sigma_x, \sigma_y, \sigma_z)$ are the Pauli matrices standing for spin or orbital freedom. $\boldsymbol{k} = (k_x, k_y, k_z)$ are the electron momentum. C_1, C_2, C_3, and k_w denote model parameters. An anisotropic second-order term $C_1(k_x^2 + k_z^2)$ is introduced to ensure the nonlinearity of the surface state dispersion (see Appendix for details). This Hamiltonian exhibits SIS with broken TRS and hosts two Weyl nodes at $\boldsymbol{k_w} = (0, 0, k_w)$ with energy $E_w = C_1 k_w^2$. The energy spectrum of the model is

$$\varepsilon = C_1(k_x^2 + k_z^2) \pm \sqrt{C_2^2(k_x^2 + k_y^2) + C_3^2(\boldsymbol{k_w^2} - \boldsymbol{k}^2)^2}, \quad (9)$$

with $\pm$ standing for the conduction and valence bands, respectively. By opening the boundary in the y direction in our model Hamiltonian and replacing k_y with $-i\partial_y$, the wave function at $k_x = k_z = 0$ could be solved. Subsequently, we project the Hamiltonian H onto the wave function to derive the effective model for the top surface states (see Appendix for details)

$$H_{\mathrm{arc}}^t = C_2 k_x + C_1(k_x^2 + k_z^2). \quad (10)$$

From Eq. (10), it is crucial that C_1 is nonzero to ensure the nonlinear dispersion of the Fermi arc. Moreover, the topological boundary conditions introduce constraint on k_x and k_z as expressed by

$$k_x^2 + k_z^2 < k_w^2, \quad (11)$$

visually represented by the red circles in Figs. 2(c) and 2(d). Similar to Eqs. (10) and (11), the bottom surface state disperses as $H_{\mathrm{arc}}^b = -C_2 k_x + C_1(k_x^2 + k_z^2)$ with the constraint $k_x^2 + k_z^2 < k_w^2$. Together with the top surface, a complete symmetrical surface band is formed as shown in Figs. 2(a) and
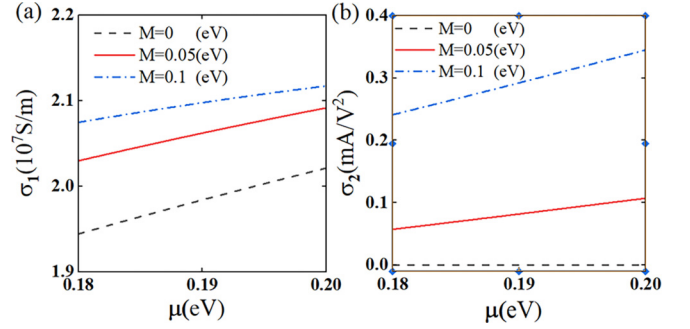

FIG. 3. Conductivities as functions of the chemical potential μ for for various bias values M at $T = 100k$ and $\tau = 10^{-11}s$. (a) shows the linear conductivity σ_1, and (b) shows the second-order nonlinear conductivity σ_2.

2(c). The effective Hamiltonian of the two band system can be expressed as

$$H_{\mathrm{eff}} = \begin{pmatrix} H_{\mathrm{arc}}^t & 0 \\ 0 & H_{\mathrm{arc}}^b \end{pmatrix} = C_1(k_x^2 + k_z^2)\boldsymbol{\tau_0} + C_2 k_x \boldsymbol{\tau_z}, \quad (12)$$

where $\boldsymbol{\tau_0}$ and $\boldsymbol{\tau_z}$ stand for the surface degrees of freedom. Note that here the surface and spin degrees of freedom are locked, and the Fermi arcs on opposite surfaces exhibit opposite spins. In experimental settings, surface state manipulation is achievable via diverse surface engineering approaches, such as truncation across distinct atomic layers [48], applying a surface gate voltage [51], or surface doping [52]. To simplify, we introduce an effective potential M on the top surface, resulting in a shift of the top energy bands (see Appendix for details):

$$H_{\mathrm{arc}}^t = C_2 k_x + C_1(k_x^2 + k_z^2) - M,$$
$$H_{\mathrm{arc}}^b = -C_2 k_x + C_1(k_x^2 + k_z^2). \quad (13)$$

This shift breaks the symmetry of the H_{eff}, resulting in asymmetry in the energy spectra of the two surfaces, as depicted in Figs. 2(b) and 2(d). The asymmetry in the bands is further reflected in the nonlinear conductivity along the x direction:

$$\sigma_1 = e^2\tau \int v_x^2\left(-\frac{\partial f_0}{\partial \varepsilon}\right)d\boldsymbol{k},$$
$$\sigma_2 = \frac{e^3\tau^2}{\hbar}\int v_x \frac{\partial v_x}{\partial k_x}\left(-\frac{\partial f_0}{\partial \varepsilon}\right)d\boldsymbol{k}. \quad (14)$$

Combining Eqs. (10) and (13) with Eq. (14), the first and second-order conductivity can be determined. The parameters used in the following text are $C_1 = 2\,\mathrm{eVnm}^2$, $C_2 = C_3 = 1\,\mathrm{eVnm}$, and $k_w = 0.3\,\mathrm{nm}^{-1}$.

III. RESULTS AND DISCUSSIONS

The conductivities σ_1 and σ_2 as functions of chemical potential under varying effective potentials are illustrated in Fig. 3. σ_1 denotes the two-dimensional Drude conductivity, which scales as

$$\sigma_1 \sim k_f^2 \sim \mu \quad (15)$$

at zero temperature. k_f is the wave vector corresponding to the Fermi energy μ. An increase in M leads to a rise in both the

Fermi wave vector and velocity at the upper surface, thereby enhancing the conductivity σ_1. The nonlinear conductivity σ_2 is illustrated in Fig. 3(b). According to Eq. (13), different surfaces contribute oppositely based on their opposite chiral Fermi velocities. Consequently, at zero temperature, σ_2 can be estimated by the difference in lengths of the two FAs shown in Fig. 2(d), which can be expanded to the first order of μ at $\mu = E_w$,

$$\sigma_2 \sim L_I^{\text{arc}} - L_{II}^{\text{arc}} \sim \sqrt{M}\mu, \tag{16}$$

where $L_{I,II}^{\text{arc}}$ are the length of the two Fermi arcs, respectively. This property opens a new route for the detection of manipulations on the FAs. As the Fermi energy increases, the FAs on the upper surface contracts more rapidly than that on the lower surface, thus amplifying the difference between them. The relationship between σ_2 and M can be similarly analyzed. σ_2 is equal to zero when M is near zero and increases as M increases.

To effectively compare the contributions of first and second-order terms in transports, we examine a Weyl nanobelt with dimensions $L_x = 10\,\mu m$, $L_z = 10\,\mu m$, and $L_y = 0.1\,\mu m$ as shown in Fig. 1(b). The thickness chosen in the y direction effectively enhances the FAs transport in the xz plane while reducing bulk band transport. To determine the nonreciprocal resistance, we apply a current along the x axis and then reverse it. Under small M, The electrical resistance can generally be described as

$$R = R_0(1 + M\gamma J), \tag{17}$$

where R_0 is the resistance at $M = 0$, and J is the electric current. The second term, dependent on the electric current, indicates nonreciprocal resistance. Note that the nonreciprocal tensor γ equals zero in systems with SIS [4]. In our model, the effect of breaking SIS is simulated by the asymmetry of the FAs, leading to a nonzero γ. The resistance difference after reversing the current direction is expressed as

$$\Delta R = R(J) - R(-J) = 2R_0 M\gamma J. \tag{18}$$

As shown in Figs. 4(a) and 4(b), the nonreciprocal resistance increases linearly with the current, and the ratio of ΔR and R is about 0.1 at $T = 100$ K, increasing with higher J, μ, and M. Given that electrons in the FAs experience reduced backward scattering, a significant nonreciprocal current difference $J(V) - J(-V)$ can be achieved by reversing a minor voltage of approximately 10 mV as shown in Fig. 4(c). The nonreciprocal signal increases with the relaxation time, which is set to a high value ($10^{-11}s$) due to the reduced backward scattering in the small M limit. Combining Eq. (17) with Eq. (2), the dimensionless nonreciprocal tensor is expressed as

$$\gamma = \frac{\sigma_2}{M\sigma_1^2}. \tag{19}$$

As shown in Fig. 4(d), γ was enhanced at high temperature and chemical potential.

It is important to note that Weyl semimetals support a topological semimetal phase (SM) for weak disorder [54–59]. An ideal 3D semimetal with Fermi energy at the Weyl points has a vanishing density of states (DOS), which is maintained at finite disorder strength. Therefore, the bulk electrons give
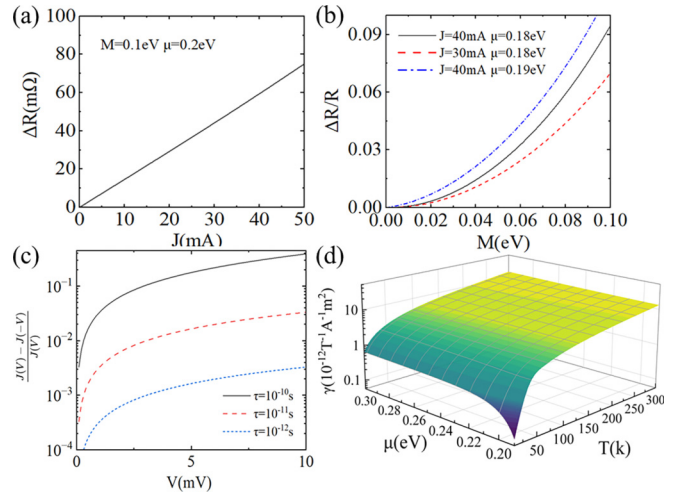

FIG. 4. Nonlinear electric transport of FAs with $\tau = 10^{-11}s$. (a) depicts ΔR as a function of the electric current, revealing a linear relationship with current J. (b) shows the ratio of nonreciprocal resistance to total resistance, varying with current and chemical potential. (c) shows the ratio of nonreciprocal current to total current, dependent on the applied potential V at varying relaxation time τ. (d) depicts γ as a function of the temperature T and the chemical potential μ with M set at 0.1 eV.

negligible contribution to the transport conductivity when the system is in the SM phase. Consequently, transport properties are predominantly contributed by the FAs, which are noted for their ultrahigh conductivity due to the low dissipation properties of Fermi arcs [23,60]. By precisely tuning the Fermi level to align with the Weyl nodes or reducing the thickness of the material, the bulk contribution is effectively reduced and surface state-dominated nonlinear nonreciprocal transport can be observed.

IV. CONCLUSION

In summary, our study presents an approach to achieve nonreciprocal transports in Weyl semimetals. This method involves the manipulation of the FAs, which introduces asymmetry in the surface energy bands without breaking spatial inversion symmetry. Employing the Boltzmann equation, we computed a range of nonreciprocal second-order responses. Compared to conventional bulk states, our approach results in a noticeable nonreciprocal current due to decreased backward scattering in the topological FAs. These findings open up possibilities for realizing nonreciprocal effects in topological materials and provide an observable signal for surface state engineering. The potential for further research into transverse effects, such as the nonlinear Hall effect and the Nernst effect, rooted in surface states, is promising and merits ongoing exploration.

APPENDIX: DERIVATION OF THE FERMI ARC SURFACE STATE

In this section, we derive the chiral FAs from the model Hamiltonian

$$H(\boldsymbol{k}) = C_1\big(k_x^2 + k_z^2\big) + C_2(k_x\sigma_x + k_y\sigma_y) + C_3\big(k_w^2 - k^2\big)\sigma_z. \tag{A1}$$

To solve the surface states, we replace k_y with $-i\frac{\partial}{\partial y}$ and obtain

$$H = C_1\big(k_x^2 + k_z^2\big) + \begin{pmatrix} C_3\big(\lambda^2 + \frac{\partial^2}{\partial y^2}\big) & C_2\big(k_x - \frac{\partial}{\partial y}\big) \\ C_2\big(k_x + \frac{\partial}{\partial y}\big) & -C_3\big(\lambda^2 + \frac{\partial^2}{\partial y^2}\big) \end{pmatrix}, \tag{A2}$$

where we have defined $\lambda = k_w^2 - (k_x^2 + k_z^2)$. Considering the following general solution

$$\phi = e^{ik_x x + ik_z z + \kappa y} \begin{pmatrix} a_1 \\ a_2 \end{pmatrix} \tag{A3}$$

to the eigenequation

$$H(\boldsymbol{k})\phi = E\phi, \tag{A4}$$

we have

$$\kappa_\alpha^2 = \frac{1}{2C_3^2}\big(C_2^2 - 2C_3^2\lambda^2 + (-1)^\alpha$$
$$\times \sqrt{C_2^4 - 4C_2^2\big(C_3^2\big(k_w^2 - k_z^2\big) + 4C_3^2\big(E - C_1 k_x^2 - C_1 k_z^2\big)^2\big)}\big), \tag{A5}$$

with $\alpha = 1, 2$ and the four degenerate states corresponding to the four solutions

$$\phi_{\alpha,\pm} = e^{ik_x x + ik_z z + \kappa_\alpha y} \begin{pmatrix} C_2(k_x \pm \kappa_\alpha) \\ E - C_3\big(\lambda^2 + \kappa_\alpha^2\big) - \big(C_1 k_x^2 - C_1 k_z^2\big) \end{pmatrix}. \tag{A6}$$

The general wave function can be written as a superposition of the four degenerate state

$$\psi_{k_x,k_z} = \Sigma_{\alpha,\pm} c_{\alpha,\pm} e^{ik_x x + ik_z z \pm \kappa_\alpha y} \phi_{\alpha,\pm}. \tag{A7}$$

For the top surface states at $y = 0$, we need

$$\psi(0) = 0 \quad and \quad \psi(-\infty) = 0, \tag{A8}$$

leading to $Re(\kappa_\alpha) > 0$ and the secular equation $det\,|\,\phi_{1,+}, \phi_{2,+}\,| = 0$. At $k_x = k_z = 0$, the wave function

$$\psi_{0,0} = (e^{\kappa_1 y} - e^{\kappa_2 y})\frac{\sqrt{2}}{2}\begin{pmatrix} 1 \\ 1 \end{pmatrix}. \tag{A9}$$

The effective Hamiltonian for the Fermi arc becomes

$$H_{\text{arc}} = \langle\,\psi_{0,0}|H|\psi_{0,0}\,\rangle$$
$$= C_2 k_x + C_1\big(k_x^2 + k_z^2\big). \tag{A10}$$

Note that since $\kappa_1\kappa_2 > 0$ (the open boundary conditions), the in plane momentum k_x, k_z of the surface states are restricted
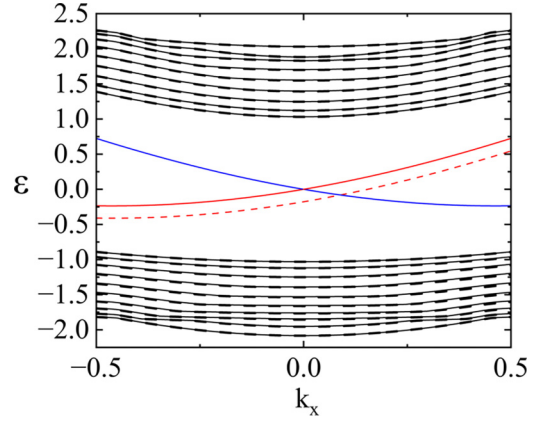

FIG. 5. The band structure at $k_z = 0$ and $M = 0.2$. Solid and dashed lines represent the band structures before and after surface doping, respectively, while red and blue lines indicate the surface states of the top and bottom surfaces, respectively. Doping causes a significant shift in the band structure of the top surface, approximately equal to the impurity strength M, while the modifications to other bands are minimal in comparison.

by the condition

$$k_x^2 + k_z^2 < k_w^2, \tag{A11}$$

which results in the fermi arc surface states. On the other hand, for the bottom surface the boundary conditions become $\psi(0) = 0$ and $\psi(\infty) = 0$. After similar analysis we found that the effective Hamiltonian for the Fermi arc and its constraint for the bottom surface can be obtained just by replacing k_x to $-k_x$ in the top surface

$$H_{\text{arc}} = -C_2 k_x + C_1\big(k_x^2 + k_z^2\big), \tag{A12}$$

$$k_x^2 + k_z^2 < k_w^2. \tag{A13}$$

To investigate the modifications of the band structure due to surface doping, we consider the following Hamiltonian of Weyl semimetal on a cubic lattice as

$$H = \sum_{\mathbf{r},\mu} t[c_{\mathbf{r}}^\dagger \sigma_z c_{\mathbf{r}+\mu} + i\delta_{\mathbf{e}_x,\mu} c_{\mathbf{r}}^\dagger \sigma_x c_{\mathbf{r}+\mu} + i\delta_{\mathbf{e}_y,\mu} c_{\mathbf{r}}^\dagger \sigma_y c_{\mathbf{r}+\mu} + \text{H.c.}]$$
$$- \sum_{\mathbf{r},\mu} t[\delta_{\mathbf{e}_x,\mu} c_{\mathbf{r}}^\dagger \sigma_0 c_{\mathbf{r}+\mu} + \delta_{\mathbf{e}_z,\mu} c_{\mathbf{r}}^\dagger \sigma_0 c_{\mathbf{r}+\mu} + \text{H.c.}]$$
$$- \sum_{\mathbf{r}} c_{\mathbf{r}}^\dagger (m\sigma_z + M\delta_{y,0}\sigma_0)c_{\mathbf{r}}, \tag{A14}$$

where $c_{\mathbf{r}}$ is a two-component spinor composed of an electron at site $\mathbf{r}$, $\mu = \mathbf{e}_x, \mathbf{e}_y, \mathbf{e}_z$ which are the unit vectors along the x, y, z directions, $\sigma_x, \sigma_y, \sigma_z$ are the Pauli matrices representing the spin degrees of freedom. $t = 0.5$ is the hopping strength, and $m = 1.8$ controls the position of the Weyl points. M denotes uniform doping at each lattice site on the top surface ($y = 0$). This Hamiltonian hosts similar band symmetries and FAs as Eq. (A1). Assuming there are ten lattice sites in the y direction, by Fourier transform of the bulk lattice-space Hamiltonian to momentum space along the x, z directions, we can obtain the band structure before and after doping as illustrated in Fig. 5 The modifications to the band structure

due to surface doping can be evaluated by the overlap integral

$$\delta\varepsilon = \int M\delta(y - 0)\psi_{\boldsymbol{k}}^2(y)dy. \qquad (A15)$$

Since the wave function of the bound states on the top surface has its maximum amplitude at $y = 0$, doping primarily affects the band structure of the top surface.

[1] Y. Tokura and N. Nagaosa, Nat. Commun. **9**, 3740 (2018).

[2] G. L. J. A. Rikken, J. Fölling, and P. Wyder, Phys. Rev. Lett. **87**, 236602 (2001).

[3] V. Krstić, S. Roth, M. Burghard, K. Kern, and G. L. J. A. Rikken, J. Chem. Phys. **117**, 11315 (2002).

[4] T. Ideue, K. Hamamoto, S. Koshikawa, M. Ezawa, S. Shimizu, Y. Kaneko, Y. Tokura, N. Nagaosa, and Y. Iwasa, Nat. Phys. **13**, 578 (2017).

[5] Y. M. Itahashi, T. Ideue, Y. Saito, S. Shimizu, T. Ouchi, T. Nojima, and Y. Iwasa, Sci. Adv. **6**, eaay9120 (2020).

[6] Y. Li, Y. Li, P. Li, B. Fang, X. Yang, Y. Wen, D.-x. Zheng, C.-h. Zhang, X. He, A. Manchon, Z.-H. Cheng, and X.-x. Zhang, Nat. Commun. **12**, 540 (2021).

[7] C. O. Avci, K. Garello, A. Ghosh, M. Gabureac, S. F. Alvarado, and P. Gambardella, Nat. Phys. **11**, 570 (2015).

[8] K. Yasuda, H. Yasuda, T. Liang, R. Yoshimi, A. Tsukazaki, K. S. Takahashi, N. Nagaosa, M. Kawasaki, and Y. Tokura, Nat. Commun. **10**, 2734 (2019).

[9] D. Choe, M.-J. Jin, S.-I. Kim, H.-J. Choi, J. Jo, I. Oh, J. Park, H. Jin, H. C. Koo, B.-C. Min, S. Hong, H.-W. Lee, S.-H. Baek, and J.-W. Yoo, Nat. Commun. **10**, 4510 (2019).

[10] S. Shim, M. Mehraeen, J. Sklenar, J. Oh, J. Gibbons, H. Saglam, A. Hoffmann, S. S.-L. Zhang, and N. Mason, Phys. Rev. X **12**, 021069 (2022).

[11] C. Ye, X. Xie, W. Lv, K. Huang, A. J. Yang, S. Jiang, X. Liu, D. Zhu, X. Qiu, M. Tong, T. Zhou, C.-H. Hsu, G. Chang, H. Lin, P. Li, K. Yang, Z. Wang, T. Jiang, and X. R. Wang, Nano Lett. **22**, 1366 (2022).

[12] K. Yasuda, T. Morimoto, R. Yoshimi, M. Mogi, A. Tsukazaki, M. Kawamura, K. S. Takahashi, M. Kawasaki, N. Nagaosa, and Y. Tokura, Nat. Nanotechnol. **15**, 831 (2020).

[13] Z. Zhang, N. Wang, N. Cao, A. Wang, X. Zhou, K. Watanabe, T. Taniguchi, B. Yan, and W. bo Gao, Nat. Commun. **13**, 6191 (2022).

[14] X. Wan, A. M. Turner, A. Vishwanath, and S. Y. Savrasov, Phys. Rev. B **83**, 205101 (2011).

[15] X. Huang, L. Zhao, Y. Long, P. Wang, D. Chen, Z. Yang, H. Liang, M. Xue, H. Weng, Z. Fang, X. Dai, and G. Chen, Phys. Rev. X **5**, 031023 (2015).

[16] A. A. Zyuzin and A. A. Burkov, Phys. Rev. B **86**, 115133 (2012).

[17] M. Hirschberger, S. Kushwaha, Z. Wang, Q. Gibson, S. Liang, C. A. Belvin, B. A. Bernevig, R. J. Cava, and N. P. Ong, Nat. Mater. **15**, 1161 (2016).

[18] P. Hosur, S. A. Parameswaran, and A. Vishwanath, Phys. Rev. Lett. **108**, 046602 (2012).

[19] Z. Wang, H. Weng, Q. Wu, X. Dai, and Z. Fang, Phys. Rev. B **88**, 125427 (2013).

[20] S. A. Parameswaran, T. Grover, D. A. Abanin, D. A. Pesin, and A. Vishwanath, Phys. Rev. X **4**, 031035 (2014).

[21] E. Liu, Y. Sun, N. Kumar, L. Muechler, A. Sun, L. Jiao, S.-Y. Yang, D. Liu, A. Liang, Q. Xu, J. Kroder, V. Süß, H. Borrmann, C. Shekhar, Z. Wang, C. Xi, W. Wang, W. Schnelle, S. Wirth, Y. Chen *et al.*, Nat. Phys. **14**, 1125 (2018).

[22] C. Shekhar, A. K. Nayak, Y. Sun, M. Schmidt, M. Nicklas, I. Leermakers, U. Zeitler, Y. Skourski, J. Wosnitza, Z. Liu, Y. Chen, W. Schnelle, H. Borrmann, Y. Grin, C. Felser, and B. Yan, Nat. Phys. **11**, 645 (2015).

[23] T. Liang, Q. Gibson, M. N. Ali, M. Liu, R. J. Cava, and N. P. Ong, Nat. Mater. **14**, 280 (2015).

[24] Y. Qi, P. G. Naumov, M. N. Ali, C. R. Rajamathi, W. Schnelle, O. Barkalov, M. Hanfland, S.-C. Wu, C. Shekhar, Y. Sun, V. Süß, M. Schmidt, U. Schwarz, E. Pippel, P. Werner, R. Hillebrand, T. Förster, E. Kampert, S. Parkin, R. J. Cava *et al.*, Nat. Commun. **7**, 11038 (2016).

[25] C.-L. Zhang, S.-Y. Xu, I. Belopolski, Z. Yuan, Z. Lin, B. Tong, G. Bian, N. Alidoust, C.-C. Lee, S.-M. Huang, T.-R. Chang, G. Chang, C.-H. Hsu, H.-T. Jeng, M. Neupane, D. S. Sanchez, H. Zheng, J. Wang, H. Lin, C. Zhang *et al.*, Nat. Commun. **7**, 10735 (2016).

[26] A. C. Potter, I. Kimchi, and A. Vishwanath, Nat. Commun. **5**, 5161 (2014).

[27] L. Luo, D. Cheng, B. Song, L.-L. Wang, C. Vaswani, P. M. Lozano, G. Gu, C. Huang, R. H. J. Kim, Z. Liu, J.-M. Park, Y. Yao, K. Ho, I. E. Perakis, Q. Li, and J. Wang, Nat. Mater. **20**, 329 (2021).

[28] A. Sekine and K. Nomura, J. Appl. Phys. **129**, 141101 (2021).

[29] G. B. Osterhoudt, L. K. Diebel, M. J. Gray, X. Yang, J. Stanco, X. Huang, B. Shen, N. Ni, P. J. W. Moll, Y. Ran, and K. S. Burch, Nat. Mater. **18**, 471 (2019).

[30] S. Dzsaber, X. Yan, M. Taupin, G. Eguchi, A. Prokofiev, T. Shiroka, P. Blaha, O. Rubel, S. E. Grefe, H.-H. Lai, Q. Si, and S. Paschen, Proc. Natl. Acad. Sci. USA **118**, e2013386118 (2021).

[31] D. Zhang, M. Shi, T. Zhu, D. Xing, H. Zhang, and J. Wang, Phys. Rev. Lett. **122**, 206401 (2019).

[32] R.-H. Li, O. G. Heinonen, A. A. Burkov, and S. S.-L. Zhang, Phys. Rev. B **103**, 045105 (2021).

[33] K. Kang, T. Li, E. Sohn, J. Shan, and K. F. Mak, Nat. Mater. **18**, 324 (2019).

[34] C. Zhang, Y. Zhang, X. Yuan, S. Lu, J. Zhang, A. Narayan, Y. Liu, H. Zhang, Z. Ni, R. Liu, E. S. Choi, A. Suslov, S. Sanvito, L. Pi, H.-Z. Lu, A. C. Potter, and F. Xiu, Nature (London) **565**, 331 (2019).

[35] O. O. Shvetsov, V. D. Esin, A. V. Timonina, N. N. Kolesnikov, and E. V. Deviatov, JETP Lett. **109**, 715 (2019).

[36] Q. Ma, S. Y. Xu, H. Shen, D. Macneill, V. Fatemi, T. R. Chang, A. Valdivia, S. Wu, Z. Du, and C. H. Hsu, Nature (London) **565**, 337 (2019).

[37] I. Sodemann and L. Fu, Phys. Rev. Lett. **115**, 216806 (2015).

[38] Y. Gao, F. Zhang, and W. Zhang, Phys. Rev. B **102**, 245116 (2020).

[39] Z. Wang, Z. Fu, P. Zhang, X.-G. Zhao, and W. Zhang, Phys. Rev. B **101**, 245313 (2020).

[40] S. Heidari and R. Asgari, Phys. Rev. B **106**, 195148 (2022).

[41] D. G. Ovalle, A. Pezo, and A. Manchon, Phys. Rev. B **106**, 214435 (2022).

[42] C. Zeng, S. Nandy, and S. Tewari, Phys. Rev. B **103**, 245119 (2021).

[43] S. Das, K. Das, and A. Agarwal, Phys. Rev. B **105**, 235408 (2022).

[44] S. Nandy, C. Zeng, and S. Tewari, Phys. Rev. B **104**, 205124 (2021).

[45] C. Zeng, S. Nandy, and S. Tewari, Phys. Rev. B **105**, 125131 (2022).

[46] C. Zeng, S. Nandy, A. Taraphder, and S. Tewari, Phys. Rev. B **100**, 245102 (2019).

[47] S. A. Ekahana, Y. W. Li, Y. Sun, H. Namiki, H. F. Yang, J. Jiang, L. X. Yang, W. J. Shi, C. F. Zhang, D. Pei, C. Chen, T. Sasagawa, C. Felser, B. H. Yan, Z. K. Liu, and Y. L. Chen, Phys. Rev. B **102**, 085126 (2020).

[48] N. Morali, R. Batabyal, P. K. Nag, E. Liu, Q. Xu, Y. Sun, B. Yan, C. Felser, N. Avraham, and H. Beidenkopf, Science **365**, 1286 (2019).

[49] S. Souma, Z. Wang, H. Kotaka, T. Sato, K. Nakayama, Y. Tanaka, H. Kimizuka, T. Takahashi, K. Yamauchi, T. Oguchi, K. Segawa, and Y. Ando, Phys. Rev. B **93**, 161112(R) (2016).

[50] Y. Sun, S.-C. Wu, and B. Yan, Phys. Rev. B **92**, 115428 (2015).

[51] Y. Zheng, W. Chen, X. Wan, and D. Y. Xing, Chin. Phys. Lett. **40**, 097301 (2023).

[52] A. Bedoya-Pinto, D. Liu, H. Tan, A. K. Pandeya, K. Chang, J. Zhang, and S. S. P. Parkin, Adv. Mater. **33**, 2008634 (2021).

[53] C. M. Wang, H.-P. Sun, H.-Z. Lu, and X. C. Xie, Phys. Rev. Lett. **119**, 136806 (2017).

[54] E. Fradkin, Phys. Rev. B **33**, 3257 (1986).

[55] K. Kobayashi, T. Ohtsuki, K.-I. Imura, and I. F. Herbut, Phys. Rev. Lett. **112**, 016402 (2014).

[56] J. H. Pixley, P. Goswami, and S. Das Sarma, Phys. Rev. B **93**, 085103 (2016).

[57] J. H. Wilson, J. H. Pixley, D. A. Huse, G. Refael, and S. Das Sarma, Phys. Rev. B **97**, 235108 (2018).

[58] Y. Ominato and M. Koshino, Phys. Rev. B **89**, 054202 (2014).

[59] B. Sbierski, G. Pohl, E. J. Bergholtz, and P. W. Brouwer, Phys. Rev. Lett. **113**, 026602 (2014).

[60] C. Zhang, Z. Ni, J. Zhang, X. Yuan, Y. Liu, Y. Zou, Z. Liao, Y. Du, A. Narayan, H. Zhang, T. Gu, X. Zhu, L. Pi, S. Sanvito, X. Han, J. Zou, Y. Shi, X. Wan, S. Y. Savrasov, and F. Xiu, Nat. Mater. **18**, 482 (2019).